Electronic supplementary materials *Mendeleev Commun*, 2024, **34**, 242–245

Low-temperature synthesis in the dittmarite–sodium acetate trihydrate system: electrochemical activity of the M^{3+}/M^{2+} redox couples in $AMPO_4$ (A = Na, Li; M = Mn, Mn/Fe)

Aleksandr Sh. Samarin, Tatiana V. Ivanova, Eugene E. Nazarov, Sergey N. Marshenya, Nikita D. Luchinin, Evgeny V. Antipov and Stanislav S. Fedotov

Experimental part

Synthesis of *dittmarite*-structured $NH_4MPO_4 \cdot H_2O$ (M = Mn, Mn/Fe). $NH_4MnPO_4 \cdot H_2O$ and $NH_4(Mn/Fe)PO_4 \cdot H_2O$ (further – precursors) were synthesized *via* a co-precipitation method. Prior to the synthesis, the water content of the crystal hydrates was measured by means of thermogravimetric analysis (TGA). In a typical procedure, $FeSO_4 \cdot 7.05H_2O$ (Komponent reactive, 98%, 4.1836 g) and $MnSO_4 \cdot 0.99H_2O$ (Komponent reactive, 98%, 10.1384 g), what refers to the expected Mn-to-Fe ratio 4:1 in the precursor, were dissolved in 80 ml of deionized H_2O (further DI H_2O; Membrane-based deionizer, BMT LLC, Russian Federation), citric acid was added to avoid the transition metals oxidation. In the case of the pure $NH_4MnPO_4 \cdot H_2O$ same ratios were used, while $FeSO_4 \cdot 7.05H_2O$ was not added. At the same time, $(NH_4)_2HPO_4$ (Ruskhim, 99%, 9.9045 g) was dissolved in the same volume of DI H_2O separately. The reactor (ORB Syrris, UK; operating volume 500 ml; equipped with an automated feeding and pH control system) was pre filled by 100 ml of ethylene glycol (EG), the feeding rate of both solutions was 1 ml min^{-1}; the suspension was continuously stirred for 12 h. The pH value was kept around 6.5 by adding ammonia or sulfuric acid solutions. The obtained sandy yellow (Mn/Fe) and pale pink (Mn) precipitates were filtered, washed, and dried in a vacuum oven at 70 °C for 12 h. Synthesis of a mixed Mn/Fe Li-based compound was performed according to the ref. S1.

Synthesis of $NaMPO_4$/C (M = Mn, Fe). The synthesis of sodium manganese/manganese-iron phosphates was conducted according to the synthesis protocol described by Koleva, Stoyanova *et al.* in the following papers.[S2,S3] The corresponding precursor and $AcONa \cdot 3H_2O$ were thoroughly mixed by mortar and pestle in a molar ratio of 1:10 with subsequent heat treatment at 200 °C (temperature increase rate of 10 or 20 °C min^{-1}) for 12 h in H_2 flow (around 2 g of mixture was used for every synthesis). Reaction can be described by the following scheme:

$$NH_4MPO_4 \cdot H_2O + Na^+ \rightarrow NaMPO_4 + H_2O\uparrow + NH_4^+$$

(with subsequent decomposition of ammonium-containing products).

The elimination of resulting volatile components from the reaction medium, such as H_2O, leads to a shift of the equilibrium towards the formation of products. After natural cooling to room temperature, the reaction products – pale yellow (Mn/Fe) or white (Mn) powders – were washed with an excessive amount of ethanol (40 °C) 5 times and dried in a vacuum oven at 70 °C for 12 h. Carbon coating was conducted according to the method described in ref. S4. For this, typically 0.7 g of the corresponding phosphate were heated in an Ar flow in the presence of glucose (1.4 g) for 12 h at 410 °C (temperature increase rate ~3 °C min^{-1}). In every case sample was cooled down naturally.

Characterization. Powder X-ray diffraction (PXRD) patterns were collected with a Bruker D8 ADVANCE powder diffractometer ($\lambda_{CuK\alpha1}$ = 1.54051 Å, $\lambda_{CuK\alpha2}$ = 1.54433 Å, equipped with an energy dispersive detector LYNXEYE XE) in Bragg–Brentano reflection geometry (0.02°, 2θ steps of 2 s/10 s for the precursors and *N*-$NaMPO_4$ respectively).

Fourier-transform infrared (FTIR) spectra were collected with an ALPHA II compact FTIR spectrometer. Spectra were recorded in the 4000–400 cm^{-1} range with 2 cm^{-1} resolution and averaging 3 scans. The reproducibility was checked by probing different spots of the same powder sample.

Scanning electron microscopy images were obtained in ThermoScientific (USA) Quattro S with an EDX Bruker (USA) XFlash 6160 detector. Presence of elements was analyzed using the QUANTAX EDS software package.

Crystal structures of both precursor and final compounds were refined from the PXRD data with TOPAS-Academic software package using the Rietveld method.[S5] For the Rietveld refinement of the mixed $Na(Mn/Fe)PO_4$ Mn and Fe occupancy values were taken according to the elemental analysis data. In other cases, atoms occupancies were found to be equal to unity. The refinement of atomic displacement parameters (ADPs) was not possible due to limitations in the XRD dataset. Specifically, this was a result of the low intensity of diffraction peaks of *d*-spacings less than 1 Å, where ADPs have the most significant influence.

The thermogravimetric and differential scanning calorimetry (TG-DSC) analysis was accomplished with the TG-DSC F3 STA-449 apparatus (Netzsch, Germany) under an 80 ml min^{-1} Ar flow and a 10 °C min^{-1} heating rate.

Electrochemical measurements. The slurry for electrode preparation was produced by mixing the active material (60%), PVDF (10%), carbon black (30%) and N-methylpyrrolidone (NMP) as a solvent in a SPEX 8000M ball mill and then applied on a carbon-coated aluminum foil using an automatic film applicator ZAA 2300 (Zehntner) with thickness of 50 μm and calendered. Round-shaped electrodes with area of 2.01 cm^2 and an average mass loading of active material of 1–2 mg cm^{-2} were cut and dried in vacuum at 120 ºC overnight. The two-electrode Swagelok-type half cells were assembled in the Ar-filled glovebox (MBraun, $p(O_2)$ = 0.1 ppm, $p(H_2O)$ = 0.1 ppm) with Na metal (Sigma Aldrich, 98%) as an anode and an electrolyte consisted of 1M $NaPF_6$ (Kishida Chemical Co. Ltd., 99.9%, was used as is) dissolved in a mixture of EC–PC (1:1 by vol.; Sigma Aldrich, >99%). For every cell 200 μl of electrolyte was used.[S6–S8] Preliminarily all solvents were dried using 4 Å molecular sieves (Sigma Aldrich). Sheets of borosilicate glass fiber were used as separators (Whatman, Cytiva). Electrochemical measurements of a Li-based composite were conducted according to the following protocol. Initially, an electrode was charged in a Na half-cell up to 4.5 V *vs.* Na^+/Na, after that the cell was quickly disassembled, the electrode was thoroughly washed with dimethyl carbonate three times in a glove box in order to remove residual Li-containing species and then was cycled in a fresh portion of electrolyte *vs.* metallic Na.[S7,S9,S10] Cycling was performed at C/20, C/10, C/5, C/2 and 1C rates. Measurements were carried out at room temperature (22 ± 1 °C) and were performed at Biologic VMP-3 potentiostat.

$NaMPO_4$ stoichiometry

In order to reduce the possible misunderstanding and excessive terminology, especially between definitions in geology and materials science, we will use the following notation for Na-bearing phosphates, taking into account the most noticeable difference between *maricite* and *triphylite* (Figure S1), which consists of the crystallographic site occupancies for light elements. While in *triphylites* Li tends to occupy the M1 site, in *maricite* the most favorable position for Na ions is the M2 site. The crystal chemistry peculiarities of this family are summarized in ref. S11.

Mn-based compound, isotypic to the $LiFePO_4$, exists in nature as a mineral *natrophilite* (all compounds isostructural to it will be labeled as $NaMPO_4$, where M refers to Mn, Fe, or a mixture thereof in the frame of this study).[S12] Another example of a composition adopting the same crystal structure is described in ref. S13. The discovered mineral represents predominantly a Mn-Fe solid

solution adopting the crystal type mentioned above. Since most of the minerals in nature are formed under hydrothermal conditions, it is reasonable to apply the same technique for the isolation of synthetic counterparts. However, by a single-step hydrothermal treatment a phase-pure $NaMnPO_4$ *natrophilite* was obtained only several times.[S14,S15] Synthetic analogs of *natrophilite* are characterized by quite limited electrochemical performance.[S16] Furthermore, all previous studies were addressing the issue of Mn-based compound synthesis, while no reports devoted to the one-step synthesis of Fe-containing *natrophilites* are known up to now. A broad set of experimental data suggests that direct heat treatment *via* the solid state or hydro-/solvo-thermal route of stoichiometric or nearly stoichiometric mixtures containing Na, Fe and phosphates inevitably leads to the formation of *maricite*s.[S17,S18] Nevertheless, great promises were expected from the Na-based analogues of $Li(Fe/Mn)PO_4$[S19–S23] which might be considered as cheap and sustainable electrode materials for SIBs. Many efforts were applied to the search for an effective and rational synthesis route of an electrochemically active $NaMPO_4$.[S6]

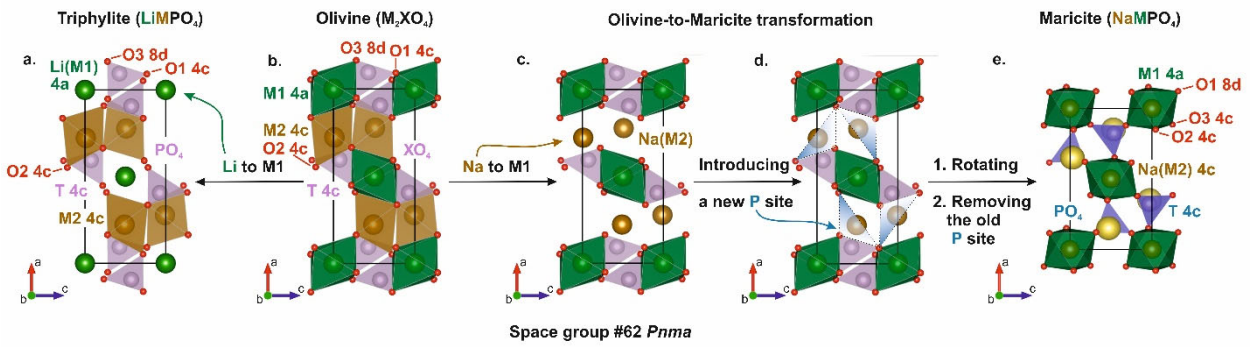

Figure S1. (**a**,**b**) Polyhedral representation of the olivine-type structures and (**c**–**e**) their conversion to the maricite type through (**c**) the introduction of Na to the M2 site and (**d**) the shift of the P position. Red spheres designate oxygen atoms; a, b, c are the unit cell directions. Adapted from ref. S11.

The *dittmarite*-to-*triphylite* transformation is determined by the great similarity between the crystal types: the same structure motif – corner-sharing MO_6 octahedra bridged by PO_4 tetrahedra – is present in both of them (*ac* and *bc* planes, respectively, Figures S1, S2)

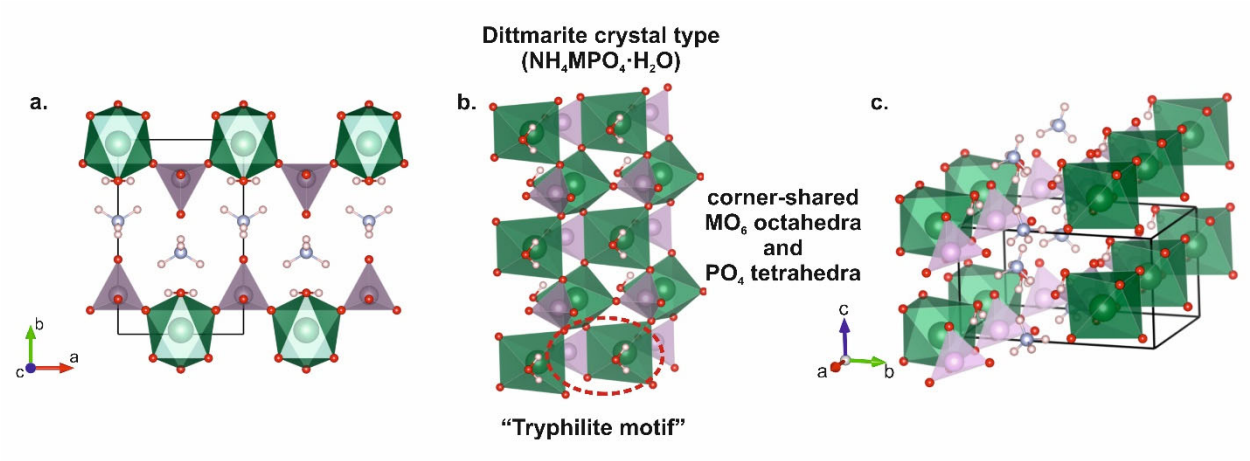

Figure S2 (**a**) Projection of the dittmarite crystal structure perpendicular to the *c* axis. (**b**) Triphylite motif in the dittmarite: corner sharing MO_6 octahedra (green) bridged by PO_4 tetrahedra (violet). (**c**) Perspective view of the dittmarite crystal structure, ammonium cations (N – light blue, H – pale pink) are located between layers.

Synthesis and crystal structure of *dittmarite*-structured precursors

According to the PXRD data (indexed in the $Pmn2_1$ space group) the co-precipitation procedure leads to the formation of phase-pure $NH_4MnPO_4 \cdot H_2O$ (a = 5.7358(3) Å, b = 8.8285(8) Å, c = 4.9143(2) Å, V = 248.86(3) Å^3) and $NH_4(Mn/Fe)PO_4 \cdot H_2O$ (a = 5.6849(7) Å, b = 8.8377(11) Å, c = 4.8726(6) Å, V = 244.81(5) Å^3) precursors (Figures S3a, b).

The co-precipitation process could be characterized by the following formulation:

$$M^{2+} + PO_4^{3-} + NH_4^+ + H_2O = NH_4MPO_4 \cdot H_2O\downarrow, \text{ where M = Mn, Fe.}$$

For the precursor synthesis, first, transition metals containing solution along with dissolved $(NH_4)_2HPO_4$ are fed into the reaction media at a constant pH value, where nucleation, crystallization, and further particle growth occur. Co-precipitation as a synthesis process allows for the production of a homogeneously distributed chemical composition both on the surface and in the bulk of materials, which is beneficial for obtaining solid solutions, especially for cathode materials, where the electrochemical performance is strictly dependent on the spatial arrangement of redox active centers.[S24] The citrate anion serves as a reducing agent, preventing oxidation of transition metals.[S25] The obtained results are in agreement with the previously reported ones on Mn/Fe-containing *dittmarites*.[S2] Another benefit of the process are mild synthesis conditions, which do not require high temperatures, pressures or high-energy mixing at all production units.

The crystal structure of $NH_4MPO_4 \cdot H_2O$ (Figure S2) is represented by a transition metal octahedra connected at the vertices in a chain stretching along the [100] direction of the unit cell, as well as reinforced with phosphate tetrahedra attached along the edge. One oxygen atom of each octahedron form hydrogen bonds with two hydrogen atoms. The ammonium groups are located in the interlayer space.[S26,S27]

Typical FTIR spectra (Figure S3c) of the obtained precursor indicate the presence of functional groups in the structure. The low-frequency part of the spectrum predominantly lights up the vibrational modes of phosphate group with bending of P–O bonds in the range of 750–500 cm^{-1} and stretching signals from 1250–1000 cm^{-1}. Between the P–O bands, a noticeable sign of water molecules vibration (librational modes) occurs. The high-frequency part of the spectrum is dominated by the N−H bonds signal, representing the NH_4^+ present in the crystal structure. The obtained result is in agreement with the reported data for $NH_4MPO_4 \cdot H_2O$.[S2,S28]

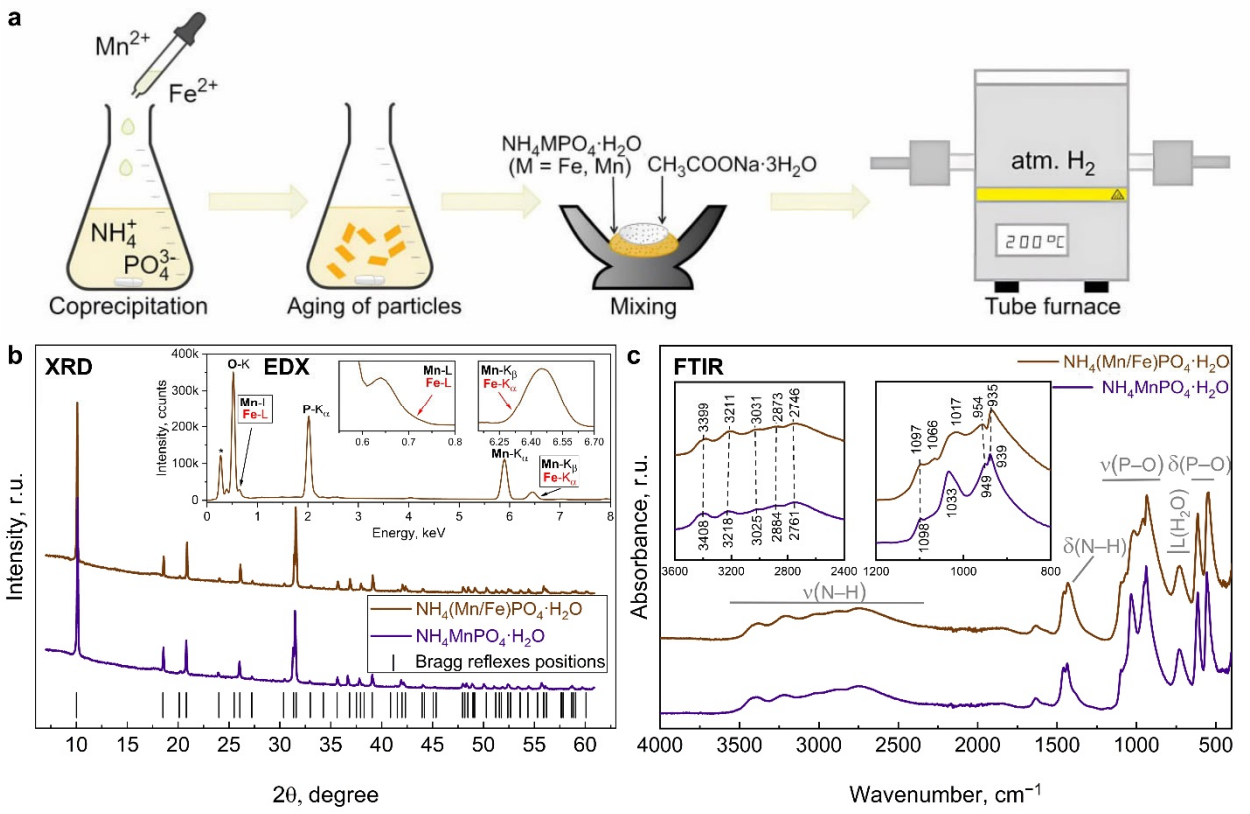

Figure S3 (**a**) Scheme of the synthesis procedure created with the use of tools by https://chemix.org. (**b**) XRD patterns of $NH_4MnPO_4·H_2O$ (violet) and $NH_4(Mn/Fe)PO_4·H_2O$ (brown) compositions. Bragg reflections are denoted as black bars. Inset: SEM-EDX spectra of $NH_4(Mn/Fe)PO_4$/C showing the presence of Fe. (**c**) FTIR spectra of $NH_4MnPO_4·H_2O$ and $NH_4(Mn/Fe)PO_4·H_2O$ in the 4000–500 cm^{-1} range. The insets show an enlarged region on stretching (left) vibrations of NH_4^+ cation and stretching (right) O–P–O vibrations.

Synthesis of $NaMPO_4$ (M = Mn, Fe)

The heat treatment in an Ar–H_2 (1% of H_2) flow of the $NH_4Mn_{0.8}Fe_{0.2}PO_4 \cdot H_2O$–$AcONa \cdot 3H_2O$ mixture reported by Koleva *et al.* leads to the formation of a non-single phase sample.[S2] This implies reducing atmosphere of pure hydrogen is favorable and applied precaution allowed to avoid oxidation of Fe^{2+}. Additionally, it is worth mentioning that phase-pure samples were obtained in our case only if the heating of a reaction mixture was conducted very fast – we suggest that the optimal temperature increase duration from RT to 200 °C should not be longer than 20 minutes.

Earlier, Boyadzhieva *et al.* deduced the set of competitive reactions that may occur in a related system, *i.e.*, $NH_4MnPO_4 \cdot H_2O$–$AcONa \cdot 3H_2O$. Heating rates, reagents' ratios and synthesis duration were investigated. For instance, heat treatment at 75 °C (1:10 reagents ratio) predominantly leads to the formation of $Mn_3(PO_4)_{2.7} \cdot H_2O$ coupled with the preservation of ~20% of the precursor and a small amount of *N*-$NaMnPO_4$. The formation of manganese phosphate hydrate may be associated with the precursor decomposition in the presence of an excessive amount of sodium ions.[S3] Further temperature increases up to 150 °C also do not allow to stabilize the desirable phase. At around 200 °C, the main product is *N*-$NaMnPO_4$, however, the formation of $NaMn_3(PO_4)(HPO_4)_2$ was observed. Further investigation of organic sodium salts-assisted topochemical and/or ion-exchange reactions may demonstrate both fundamental and practical interest in an area of Na-containing compounds synthesis as electrode materials for metal-ion batteries.[S29–S31] Moreover, low-melting temperature sodium salts could be applied not only as reagents but also as flux components, facilitating the target growth of the desirable phase during dissolution–crystallization processes at elevated temperatures.[S32,S33]

Table S1 Atomic positions and fractional coordinates for $NaMnPO_4$.

Atom	Wyckoff	*x/a*	*y/b*	*z/c*	Occupancy
Na1	4*a*	0	0	0	1
Mn1	4*c*	0.2848(2)	¼	0	1
P1	4*c*	0.1097(3)	½	0.4416(6)	1
O1	4*c*	0.1077(8)	¼	¾	1
O2	4*c*	0.4715(7)	¼	0.1568(15)	1
O3	8*d*	0.1753(5)	0.0576(8)	0.3119(13)	1

Table S2 Atomic positions and fractional coordinates for Na(Mn/Fe)PO_4.

Atom	Wyckoff	*x/a*	*y/b*	*z/c*	Occupancy
Na1	4*a*	0	0	0	1
M1	4*c*	0.2849(2)	¼	0	1*
P1	4*c*	0.1105(5)	¼	0.4408(8)	1
O1	4*c*	0.1093(9)	¼	¾	1
O2	4*c*	0.4716(7)	¼	0.1590(6)	1
O3	8*d*	0.1757(8)	0.0579(9)	0.3101(15)	1

* M1 label refers to the site occupied by Mn and Fe atoms.

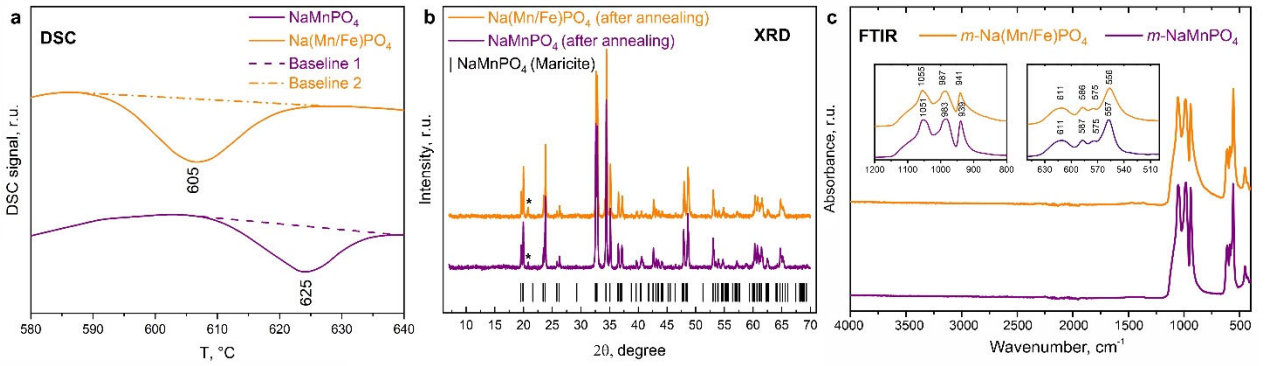

Figure S4 (**a**) DSC curves of $NaMPO_4$ (M = Mn, Mn/Fe) in the 580–640 °C temperature range showing endothermic processes at 605 and 625 °C for $NaMnPO_4$ and Na(Mn/Fe)PO_4, respectively. (**b**) Phase analysis of products of thermal transformation of $NaMPO_4$ samples. Symbol * designates the reflection which corresponds to the impurity. Bragg reflections of *maricite* are denoted as bars below. (**c**) FTIR spectra of *m*-$NaMPO_4$ (M = Fe, Mn) in the 4000–500 cm^{-1} range. The insets show enlarged regions on stretching (left) and bending (right) vibrations of P–O bonds.

Notes about the delithiation of Mn-rich frameworks

Experimental data of chemical deinsertion of alkali metal cations also suggest that Mn-rich frameworks reveal a tendency to preserve a non-negligible residual amount of Li^+/Na^+ ions in the channels. In particular, Henriksen *et al.* used 1.5 eq. of nitronium tetrafluoroborate (NO_2BF_4) in acetonitrile (10 ml per 100 mg of phosphate) to prepare fully delithiated samples, whose purity was confirmed by PXRD and pair distribution function analyses. Noteworthy, the drying step was conducted under inert atmosphere.[S27] The authors mention that 'materials with $y = 0.6–0.8$ (Mn content) yields somewhat lower capacities'. Similar to our observations, the initial discharge capacity of '$Fe_{0.2}Mn_{0.8}PO_4$' in that experiment is about 30% higher than those of subsequent cycles. Thus, we can assume that oxidized samples tend to compensate the energetically unfavorable Mn^{3+}-enriched state by a partly irreversible alkali metal cation intercalation or by a reaction with protons. This could explain why even in the aqueous media the use of persulfates does not allow to isolate phase-pure samples. Cascades of processes associated with Mn^{3+}-rich framework decomposition were recently investigated by Huang, Chernova *et al*.[S34] Briefly, residual water content in an aprotic solvent leads to transformation of $MnPO_4$ to amorphous $MnHP_2O_7$ and further $MnH_2P_2O_7$.

Notes about theoretical studies of $NaMPO_4$

Several studies addressed issues of the computational analysis of $NaMPO_4$ compounds isostructural to the $LiFePO_4$. In particular, Tripathi *et al.* pointed out the effect of the unit cells' volumes mismatch.[S35] The volumes' difference (ΔV) between fully sodiated and fully deintercalated phases is 17% and 20% for pure Fe- and Mn-based frameworks, respectively. The formation of a phase boundary between oxidized and reduced phases during deinsertion/insertion impose an additional activation energy barrier, which in turn corresponds to the propagation of the phase front within the particles.[S22,S35] The strain generated is proportional to the ΔV. In principle, electrochemical performance is controlled by the amount of strain generated phase boundaries as well as by the activation energy barrier (E_a) for ion transport. Later, Zhu *et al.* focused on $NaMnPO_4$. According to the DFT simulations Mn-based *natrophilite* is characterized by a quite high ionic migration energy value (0.41 eV along [010]).[S36,S37] The authors stated that 'slightly lower electronic conduction in the sodiated phase and ion conduction in the desodiated phase are not conductive to high-rate performance' and additionally predicted the structural instability of partly desodiated $NaMnPO_4$. In all, there is still a room for further improvement in theoretical and experimental investigation of $NaMPO_4$.

References

S1 C. Wu, J. Xie, G. Cao, X. Zhao and S. Zhang, *CrystEngComm*, 2014, **16**, 2239.

S2 V. G. Koleva, T. J. Boyadzhieva and R. K. Stoyanova, *Cryst. Growth Des.*, 2019, **19**, 3744.

S3 T. Boyadzhieva, V. Koleva and R. Stoyanova, *Bulg. Chem. Commun*, 2013, **45** (Special Issue B), 208.

S4 R. Tian, H. Liu, Y. Jiang, J. Chen, X. Tan, G. Liu, L. Zhang, X. Gu, Y. Guo, H. Wang, L. Sun and W. Chu, *ACS Appl. Mater. Interfaces*, 2015, **7**, 11377.

S5 A. A. Coelho, *J. Appl. Crystallogr.*, 2018, **51**, 210.

S6 C. Henriksen, J. K. Mathiesen, Y.-M. Chiang, K. M. Ø. Jensen and D. B. Ravnsbæk, *ACS Appl. Energy Mater.*, 2019, **2**, 8060.

S7 T. J. Boyadzhieva, V. G. Koleva, R. R. Kukeva and R. K. Stoyanova, *ACS Appl. Energy Mater.*, 2021, **4**, 7182.

S8 V. Koleva, M. Kalapsazova, D. Marinova, S. Harizanova and R. Stoyanova, *ChemSusChem*, 2023, **16**, e202201442.

S9 T. Boyadzhieva, V. Koleva, P. Markov and R. Stoyanova, *Dalton Trans.*, 2021, **50**, 16548.

S10 T. Boyadzhieva, V. Koleva, R. Kukeva, D. Nihtianova, S. Harizanova and R. Stoyanova, *RSC Adv.*, 2020, **10**, 29051.

S11 E. E. Nazarov, D. A. Aksyonov, E. V. Antipov and S. S. Fedotov, *Energies*, 2023, **16**, 5083.

S12 P. B. Moore, *Am. Mineral.*, 1972, **57**, 1333.

S13 P. Vignola, F. Hatert, A.-M. Fransolet, O. Medenbach, V. Diella and S. Ando, *Am. Mineral.*, 2013, **98**, 767.

S14 S. Jana, G. Lingannan, M. Ishtiyak, G. Panigrahi, A. Sonachalam and J. Prakash, *Mater. Res. Bull.*, 2020, **126**, 110835.

S15 M.-Y. Pan, S.-T. Lu, M.-Y. Zhang, C. Li, G.-D. Zou, K.-Z. Cao and Y. Fan, *J. Solid State Chem.*, 2023, **321**, 123929.

S16 T. Boyadzhieva, V. Koleva, E. Zhecheva, D. Nihtianova, L. Mihaylov and R. Stoyanova, *RSC Adv.*, 2015, **5**, 87694.

S17 V. Koleva, T. Boyadzhieva, E. Zhecheva, D. Nihtianova, S. Simova, G. Tyuliev and R. Stoyanova, *CrystEngComm*, 2013, **15**, 9080.

S18 M. G. Mestres, M. Casas-Cabanas, A. Guerfi, M. Armand, T. Rojo, K. Zaghib and A. Paolella, US Patent 11569506 B2, 2023.

S19 E. E. Nazarov, A. D. Dembitskiy, I. A. Trussov, O. A. Tyablikov, I. S. Glazkova, A. V. Sobolev, I. A. Presniakov, I. V. Mikheev, A. V. Morozov, V. A. Nikitina, A. M. Abakumov, E. V. Antipov and S. S. Fedotov, *Energy Adv.*, 2023, **2**, 328.

S20 E. E. Nazarov, O. A. Tyablikov, V. A. Nikitina, E. V. Antipov and S. S. Fedotov, *Applied Nano*, 2023, **4**, 25.

S21 R. V. Apraksin, S. N. Eliseeva, E. G. Tolstopjatova, A. M. Rumyantsev, V. V. Zhdanov and V. V. Kondratiev, *Mater. Lett.*, 2016, **176**, 248.

S22 O. A. Drozhzhin, V. D. Sumanov, O. M. Karakulina, A. M. Abakumov, J. Hadermann, A. N. Baranov, K. J. Stevenson and E. V. Antipov, *Electrochim. Acta*, 2016, **191**, 149.

S23 R. V. Apraksin, S. N. Eliseeva, M. A. Kamenskii, E. G. Tolstopyatova, G. G. Lang and V. V. Kondrat'ev, *Russ. J. Electrochem.*, 2019, **55**, 1047 (*Elektrokhimiya*, 2019, **55**, 1295).

S24 H. Dong and G. M. Koenig, *CrystEngComm*, 2020, **22**, 1514.

S25 M.-S. Kim, J.-P. Jegal, K. C. Roh and K.-B. Kim, *J. Mater. Chem. A*, 2014, **2**, 10607.

S26 G. V. Kiriukhina, O. V. Yakubovich and O. V. Dimitrova, *Crystallogr. Rep.*, 2015, **60**, 198 (*Kristallografiya*, 2015, **60**, 221).
S27 O. V. Yakubovich, O. V. Karimova, O. K. Mel'nikov and V. S. Urusov, *Dokl. Akad. Nauk (Proc. Acad. Sci. USSR)*, 1995, **342**, 40 (in Russian).
S28 V. G. Koleva, *Spectrochim. Acta, Part A*, 2007, **66**, 413.
S29 S. D. Shraer, N. D. Luchinin, I. A. Trussov, D. A. Aksyonov, A. V. Morozov, S. V. Ryazantsev, A. R. Iarchuk, P. A. Morozova, V. A. Nikitina, K. J. Stevenson, E. V. Antipov, A. M. Abakumov and S. S. Fedotov, *Nat. Commun.*, 2022, **13**, 4097.
S30 A. Sh. Samarin, A. V. Ivanov and S. S. Fedotov, *Clean Technologies*, 2023, **5**, 881.
S31 A. I. Komayko, S. D. Shraer, S. S. Fedotov and V. A. Nikitina, *ACS Appl. Mater. Interfaces*, 2023, **15**, 43767.
S32 I. A. Moiseev, A. A. Savina, A. D. Pavlova, T. A. Abakumova, V. S. Gorshkov, E. M. Pazhetnov and A. M. Abakumov, *Energy Adv.*, 2022, **1**, 677.
S33 A. A. Savina, A. O. Boev, E. D. Orlova, A. V. Morozov and A. M. Abakumov, *Russ. Chem. Rev.*, 2023, **92**, RCR5086 (*Usp. Khim.*, 2023, **92**, RCR5086).
S34 Y. Huang, N. A. Chernova, Q. Yin, Q. Wang, N. F. Quackenbush, M. Leskes, J. Fang, F. Omenya, R. Zhang, M. J. Wahila, L. F. J. Piper, G. Zhou, C. P. Grey and M. S. Whittingham, *Inorg. Chem.*, 2016, **55**, 4335.
S35 R. Tripathi, S. M. Wood, M. S. Islam and L. F. Nazar, *Energy Environ. Sci.*, 2013, **6**, 2257.
S36 L. Zhu, L. Li, J. Wen and Y.-R. Zeng, *J. Power Sources*, 2019, **438**, 227016.
S37 L. Zhu, J.-Y. Xie, G.-M. Zhou, D.-A. Zhang and A. Du, *Solid State Ionics*, 2023, **398**, 116274.